Electrified deep convection and rare lightning events infer rapid intensification during Hurricane Nicholas (2021)

Timothy Logan[1*], Jacob Hale[1], Sydney Butler[1], Brendan Lawrence[1], and Samuel Gardner[2]

[1] Texas A&M University, College Station, Texas

[2] Texas Tech University, Lubbock, Texas

Submitted to *Journal of Earth and Space Science*

Corresponding author address: Dr. Timothy Logan, the Department of Atmospheric Sciences, Texas A&M University, 3150 TAMU, College Station, TX 77843-3150. Email: tlogan52@tamu.edu, 979-845-2004.

Abstract

Hurricane Nicholas was classified as a Category 1 tropical cyclone (TC) at 0000 UTC on 14 September 2021 and made landfall along the upper Texas Gulf Coast at 0530 UTC. The sustained maximum wind speed increased from a low-end estimate of 13 m s^{-1} (0000 UTC 13 September) to 33 m s^{-1} (0000 UTC 14 September) indicating rapid intensification. Lightning activity, monitored by the Houston Lightning Mapping Array (HLMA), developed in the rainband at 1700 UTC on 13 September, diminished by 2030 UTC, and re-intensified after 2200 UTC. At 2004 UTC (13 September), a curved megaflash (~220 km) was observed in the outer rainband's stratiform precipitation region. Convection developed and intensified in the eastern eyewall region by 0130 UTC on 14 September. Several transient luminous events (TLEs) were observed in the western eyewall region between 0230-0300 UTC with VHF source points exceeding 40 km during a decline in lightning activity. The TLEs occurred during a period of strong cloud top divergence resulting from complex interactions between southwesterly low-level and westerly deep layer wind shear. Charge analysis of Nicholas revealed an overall normal dipole structure, while the megaflash and TLE cases exhibited inverted charge structures. The upper-level screening and primary charge layer heights of the TLEs heavily influenced the VHF source altitudes. Interestingly, a surface wind gust of 42 m^2 s^{-2} was observed near the time of the first TLE, suggesting a second period of brief intensification. Future investigations of TC evolution and behavior may benefit from charge analyses.

Keywords: atmospheric electricity (3304), lightning (3324), tropical cyclones (3372), tropical convection (3371), instruments and techniques (3394)

Key Points

- Wind shear and thermodynamic conditions modulate the location and magnitude of lightning activity during Hurricane Nicholas.
- Rainband and eyewall lightning activity and charge structure yield clues about Nicholas' intensification.
- A megaflash was observed before and several transient luminous events were observed after Nicholas' transition to a hurricane.

Plain Language Summary

Hurricane Nicholas rapidly intensified and impacted the Texas Gulf Coast just after midnight on 14 September 2021. Nicholas moved inland southwest of Houston and rapidly weakened throughout the day. Powerful low- and mid-level winds blew counterclockwise around the eye while upper-level winds were blowing from the southwest. This created wind shear and removal of upper-level air, or divergence, which helped to intensify updrafts and thunderstorm development in the rainband and eyewall. The Houston Lightning Mapping Array, a network of lightning detectors, identified frequent lightning activity within the rainband a few hours before Nicholas became a hurricane. The thunderstorms in the rainband produced a large, curved "megaflash" that was 220 km across. Vigorous eyewall lightning activity was observed a few hours Nicholas was designated as a hurricane. The thunderstorms in the eyewall produced rarely observed lightning, called transient luminous events. This type of lightning travels upwards from the tops of the thunderclouds towards space. The wind shear along with the timing and location of the lightning events gave important clues about Nicholas' intensification. The results of this study can be used in future efforts to investigate hurricane strengthening and potential impacts.

1. Introduction

Electrified convection that develops within tropical cyclones (TCs) can give indications on the evolution of timing, track, and intensity (Logan, 2021; Solorzano et al., 2018; Xu et al., 2017). Rapid intensification (RI) occurs when a TC experiences a 15 m s^{-1} (30 kt) or greater wind increase in the span of 24 hours (Kaplan & DeMaria, 2003). In contrast, rapid weakening (RW) occurs when a TC experiences a 15 m s^{-1} decrease within 24 hours (Wood & Ritchie, 2015). A sudden increase and decline in lightning within the eyewall of Harvey was noted during a period of rapid intensification prior to landfall along the Texas Gulf Coast as a Category 4 hurricane by Logan (2021). In addition, there was a lag of several hours in the temporal relationship between the increase in rainband lightning activity and devastating flooding that occurred in Houston. However, many studies present conflicting results when regarding the relationship between lightning and RI/RW (DeMaria et al., 2012; Frank & Ritchie 2001; Solorzano et al., 2018; Stevenson et al., 2014; Stevenson et al., 2016; Wood & Ritchie 2015).

The Logan (2021) study employed a lightning mapping array (LMA) centered in Houston (HLMA). LMAs retrieve spatial and temporal information of total lightning in electrified deep convection as well as the altitudes of lightning sources and charge layer polarity (Rison et al., 1999; Logan, 2021; Medina et al., 2021). If information about the height of a charge layer is known, then inferences can be made about the microphysics of the deep convective clouds (Boggs et al., 2018; Liu et al., 2015; Lu et al., 2011; Schultz et al., 2015; Tessendorf et al., 2007; Wiens et al., 2005). As an added advantage, LMAs can resolve small scale temporal electrified convective features faster than radar, satellite, and other measurement platforms (Steiger et al., 2007; Tessendorf et al., 2007). However, it is important to note that LMAs have a limited range of detection and location errors increase with the square of the distance between the source and

detector beyond 100 km (Cullen, 2013; Krehbiel et al., 1999; Rison et al., 1999; Weiss et al., 2018). Nevertheless, when a TC develops in the vicinity of an LMA, it is possible to illustrate the lightning behavior and charge structure of electrified convection (Liu et al., 2015; Logan, 2021).

Nicholas was designated as a Category 1 hurricane by the National Hurricane Center (NHC) at 0000 UTC on 14 September 2021 with a maximum sustained wind speed of speed of 33 m s^{-1} (65 kt) (Latto & Berg, 2022). The winds prior to the upgrade were sustained at 20 m s^{-1} (40 kt) for at least 24 hours, which nearly fits the criteria of a rapidly-intensifying TC. However, according the NHC tropical cyclone report, it is possible that Nicholas rapidly intensified because the best fit method used to estimate wind strength included wind speed measurements of at least 13 m s^{-1} (25 kt) (see Figure 2 of Latto & Berg 2022). Hence, this study assumes that RI occurred from 0000 UTC 13 September to 0000 UTC 14 September.

Not only did Nicholas exhibit frequent electrified convection for a substantial portion of its life cycle, but additionally, two notable features were well captured by the HLMA: (i) what appeared to be a curved megaflash on 13 September and (ii) several high-altitude "jet-like" transient luminous events (TLEs) on 14 September. A megaflash is defined as a lightning flash which has an extent of 100 km or greater (Peterson, 2021; Peterson et al., 2022; Peterson, 2023). Megaflashes typically occur in the stratiform region during a transition of a deep convective event to a mesoscale convective system (MCS) and initiate in and around regions of low-level (< 7 km) positive charge or inverted charge structures (Lyons et al., 2020; Peterson, 2023). The causes of how megaflashes occur and their electrical nature are still under much debate, especially considering recent discoveries of the longest lightning flashes in the world (Lyons et al., 2020; Peterson et al., 2021; Peterson et al., 2022). Hence, observing one during a tropical cyclone event is nearly unprecedented. However, Lyons et al. (2020) and Peterson (2023) pointed out that

megaflashes may not be uncommon given the recent advent of sophisticated space-based lightning detection sensors (e.g., Geostationary Operational Environmental Satellite (GOES) geostationary lightning mapper (GLM)).

Jets (e.g., blue and gigantic jets) are TLEs which occur just above the cloud tops of vigorous thunderstorms (Boggs et al., 2022). In particular, gigantic jets tend to occur more so over maritime than continental deep convection (Boggs et al., 2018; Boggs et al., 2022; Lu et al., 2011; Liu et al., 2015). They are typically observed during a period of decreasing lightning flash rates with a corresponding uptick in charge layer height, and can also indicate TC intensification (Boggs et al., 2018; Liu et al., 2015). High-altitude electrical activity (i.e., charge layer altitudes exceeding 15 km) typically denotes a complex mixture of deep convective cloud dynamics and microphysics, such as ice particles with broad size distributions, strong turbulent updrafts, cloud top divergence in the vicinity of the updraft, and wind shear (Boggs et al., 2018; Boggs et al., 2022, Takahashi, 1978). The dynamic motions can enhance ice particle collisions necessary for charging in the presence of supercooled liquid water (e.g., non-inductive charge mechanism) (Boggs et al., 2018; Wang et al., 2018; Wang et al., 2021).

This study employs measurements from the HLMA along with additional lightning, meteorological, satellite, and radar products to address the following scientific questions:

(1) How can rapid intensification be identified by electrified deep convective behavior with respect to the meteorological conditions during the life cycle of Nicholas?

(2) How can charge structure information be used to elucidate not only the strengthening and weakening of Nicholas but also the observed rare lightning events?

The location of lightning activity within a tropical cyclone can denote changes in convective strength (DeMaria et al., 2012; Solorzano et al., 2018; Stevenson et al., 2014; Wadler et al., 2022). Strong indicators of where lightning activity is preferentially located are related to factors such as the motion of the TC with respect to the orientation and magnitude of low-level shear (1000-850 hPa), deep layer shear (1000-250 hPa), and mean low-level wind (850 hPa) vectors (Chen et al., 2006; Corbosiero & Molinari, 2002; Corbosiero & Molinari, 2003; Didlake & Kumjian, 2017; Frank & Ritchie, 2001; Homeyer et al., 2021; Latto & Berg, 2022; Stevenson et al., 2016; Wadler et al., 2022). Hence, an analysis of the dynamic environment is performed to explain lightning behavior during Nicholas.

Logan (2021) and Pan et al. (2020) lacked a robust charge analysis of tropical deep convection during Harvey. Though no TLEs or other anomalous lightning features were detected by the HLMA near the Texas Gulf Coast, Wang et al. (2021) showed that several TLEs were observed (e.g., red sprites and gigantic jets) while Harvey was positioned in the Caribbean Sea. Furthermore, the TLEs imply the presence of an extensive upper-level negative charge layer which screens an underlying positive layer (Boggs et al., 2018; Boggs et al., 2022). Liu et al. (2015) suggested that erosion of the negative screening layer due to upper-level divergence can aid in negative leaders escaping upward to the ionosphere, as observed during Hurricane Dorian. Hence, this study adopts the methodologies of Liu et al. (2015), Boggs et al. (2018), and Boggs et al. (2022) along with a charge analysis following the method of Medina et al. (2021) to evaluate the charge layer characteristics of the rainband and eyewall convection.

2. Data and Methodology

2.1 Houston Lightning Mapping Array (HLMA)

The Houston Lightning Mapping Array (HLMA) consists of a network of very high frequency (VHF) time-of-arrival (TOA) lightning mapping sensors. The sensor network encompasses the entirety of the Houston metropolitan area and can detect nearly 100% of total lightning occurring within a 100-km radius from the centroid (29.76°N, 95.37°W) (Cullen, 2013; Logan, 2021). The HLMA network has undergone upgrades (e.g., addition of sensors and hardware improvements) since 2020 which has helped to extend the detection of VHF source points to nearly 400 km from the HLMA centroid with a detection efficiency exceeding 70% up to 250 km (see Figure 1 in Logan, 2021). Note that this also includes increased coverage over the remote Gulf of Mexico. The uncertainty of VHF source detection rapidly increases as the square of the range away from the centroid increases (Thomas et al., 2004). Two factors to consider regarding source points located much greater than 100 km away from the centroid are (a) number of detectable VHF sources located high up in the deep convective cloud and (b) at least five sensors need to detect the VHF sources to be processed as a legitimate data point. Hence, the detection efficiency of VHF sources is highly contingent upon the robustness of the deep convection and VHF source point emission.

Lightning mapping software such as XLMA is used to manually analyze the charge structure of VHF source data retrieved by the sensors (Thomas et al., 2004). The leader initiating the flash propagates through regions of positive and negative charge. Positive charge regions (negative leaders) are “noisier” than negative charge regions (positive leaders) and can be subjectively identified using XLMA, lightning flash polarity, and peak current from platforms such as the National Lightning Detection Network (NLDN) (Cummins et al., 1998). Thunderstorms can have anywhere from a few dozen to thousands of flashes per hour, which proves to be a tedious task to analyze manually. The number of VHF source points constituting flash size can be sorted

by XLMA to discern big, medium, and small flashes. Hence, for a deep convective event with thousands to millions of source points, it is expedient to analyze the charge structure using big flashes. However, it is possible to lose a great deal of information about the storm evolution since big flashes are only observed during certain periods in a convective event.

The raw VHF source data are quality controlled by using XLMA to remove questionable and mislocated source points using the chi-square parameter (χ^2) which can minimize errors in geolocating the sources (Thomas et al., 2004). However, it is likely that TLEs and other anomalous lightning events may be hidden in what is considered erroneous VHF source data. Thus, this study incorporates the following criteria: (a) the χ^2 value is set to 2 to ensure location and timing accuracy and (b) the minimum number of HLMA sensors is set to 7 to ensure enough sensors observed the same VHF source events for better data quality (Lyons et al., 2020).

The VHF source data are then sorted into flash groups using algorithms developed by Bruning & MacGorman, (2013) and Fuchs et al. (2015) (e.g., "lmatools" Python-based software package). These algorithms constitute VHF lightning sources within 3 km and 0.15 s of one another into a flash and can differentiate between other sources and flashes. Note that this study will use both VHF source (primary TC analysis) and flash level data (secondary charge layer analysis) as proxies for dynamical and microphysical which are detailed further in the following sections. Upper atmosphere VHF source points (>15 km) can sometimes be identified as mislocated pulses above the cloud top. Therefore, observed VHF sources above 20 km that are not eliminated by quality control filtering are included in this study (Boggs et al., 2022).

2.2 Charge Analysis

A typical thunderstorm will have at least two charge layers depending on the direction of propagation of the negative or positive leader after initiation (Chmielewski et al., 2018; Medina et al., 2021; Williams, 1985). A normal dipole charge layer consists of an upper-level positive charge overlying a negative charge layer, while an inverted dipole is opposite (Stolzenburg & Marshall, 2009). A tripole has three charge layers with normal being a negative layer sandwiched between two positives, with an inverted tripole being the opposite (Stolzenburg & Marshall, 2009). Therefore, dipole and tripole charge structures can indicate possible abnormalities during a thunderstorm's life cycle (Tessendorf et al., 2007).

ChargePol is an objective, automated method which uses LMA flash level data to determine lightning flash polarity, charge layer altitude, and vertical distribution of charge layers during the life cycle of electrified deep convection (Medina et al., 2021). Not only does ChargePol greatly reduce the analysis time of lightning flashes, but it can also estimate the altitude and thickness of positive and negative charge layers. ChargePol data is incorporated into XLMA in this study, which offers an advantageous opportunity to dissect the electrical nature of individual cells, individual cells within a group of storms, or an entire deep convective event. This aids in assessing which specific areas of deep convection in the TC contribute most to RI or RW.

2.3 NEXRAD

Deep convective clouds can be well illustrated by radar reflectivity (Fridlind et al., 2019; Steiger et al., 2007). Lightning activity is generally inferred by the presence of the 30 dBZ echo layer typically at a height several kilometers above the melting level (Carey & Rutledge, 2000; Logan, 2021; Petersen & Rutledge, 2001; Stolz et al., 2014; Wang et al., 2018). At this altitude, it is assumed that there is an abundance of supercooled liquid water and mixed populations of large and small ice particles (e.g., hail, graupel, snow, rimed ice, etc.). The ice particles will collide and

exchange charges as long as the environmental temperature is between -10°C and -40°C (Mecikalski et al., 2015). Given updraft speeds exceeding 20 m s^{-1}, sufficient turbulence in tropical convection (e.g., Cecil & Zipser, 1999) will carry smaller positively charge ice particles to upper regions of the deep convective cloud while larger ice particles will fall to the base of the cloud facilitating a negative charge ultimately leading to a lightning discharge (e.g., cloud-to-ground or intracloud).

Therefore, Next Generation Radar (NEXRAD) products are used in this study to illustrate the spatiotemporal evolution and movement of hydrometeors in electrified convection (Crum & Alberty, 1993). The products include base reflectivity (Z_h) and derived products such as cloud echo top height and radial divergence. A gridded NEXRAD product (GridRad) is utilized to analyze the cross-section altitude of the radar scans in relation to the HLMA observations of charge layers (Homeyer & Bowman, 2017). GridRad features a 5-min temporal resolution along with a spatial resolution of (0.02º x 0.02º x 1 km). VHF source points can be easily overlain onto the plan and cross-section GridRad plots to better illustrate the 4-dimensional (4-D, e.g., longitude, latitude, altitude, and time) electrical and microphysical nature of deep convection (Logan, 2021).

2.4 Meteorological Analysis

The environmental conditions that facilitate charging in a TC are complex and extensively researched (Black & Hallett, 1986; Cecil & Zipser, 1999; Cecil et al., 2002; DeHart & Bell, 2020; Fierro et al., 2015; Fierro & Mansell, 2017; Frank & Ritchie, 2001; Han et al., 2021; Hu et al., 2020; Leighton et al., 2020; Wood & Ritchie, 2015). A reason certain TCs exhibit more lightning than others may be explained by the degree of updraft strength, wind shear, and influence of synoptic boundaries which advect moist parcels and enhance supercooled liquid water amount and

ice-ice collisions (Cecil & Zipser, 1999). It is likely that supercooled liquid water plays a significant role as a limiting factor in the electrification of many TCs.

Therefore, it is necessary to include data regarding environmental dynamic/thermodynamic conditions during the evolution of Nicholas. Data products include environmental and dewpoint temperature profiles, surface and most unstable (MU) convective available potential energy (CAPE), wind speed and direction profiles, low-level (surface to 1 km) and deep layer (surface to 8 km) wind shear, and storm relative helicity (SRH). Since Nicholas intensified and made landfall primarily between Corpus Christi (CRP) and Lake Charles (LCH), National Weather Service (NWS) soundings at those locations along with rapid refresh (RAP) soundings are used to further examine the environmental conditions relative to areas of rainband and eyewall convection. Furthermore, special attention is paid to the environmental conditions during the megaflash and TLE cases. Note that the NHC Tropical Cyclone Report (Latto & Berg, 2022) is used as ground truth for the timing of the TC stages from tropical storm to hurricane status, the location of the eye/eyewall, wind speed, and central pressure for Nicholas.

3. Results

3.1 Summary of initial development

According to Latto & Berg (2022), Nicholas was disorganized when it initially developed. The TC was steered northward by a subtropical ridge located in the eastern Gulf of Mexico. There was ongoing convection along the Texas/Louisiana Gulf Coast that was likely a mixture of weak continental and tropical convection prior to 1200 UTC on 12 September 2021. At 1200 UTC, Nicholas was officially designated as a tropical storm and the transition to strongly-forced TC convection was abrupt (see Figures 1a and 1c – black line). By 0000 UTC on 13 September 2021,

Nicholas had redeveloped twice and moved northeastward as the ridge began to weaken. There was never an observable eye with Nicholas from GOES satellite imagery (Supplemental Movie 1), but GridRad reflectivity data revealed discernible eyewall convection and structure by 1700 UTC as Nicholas moved closer to the Texas Gulf Coast within the range of the Houston (KHGX) and Corpus Christi (KCRP) radar platforms (Supplemental Movie 1).

3.2 Electrified nature of Nicholas

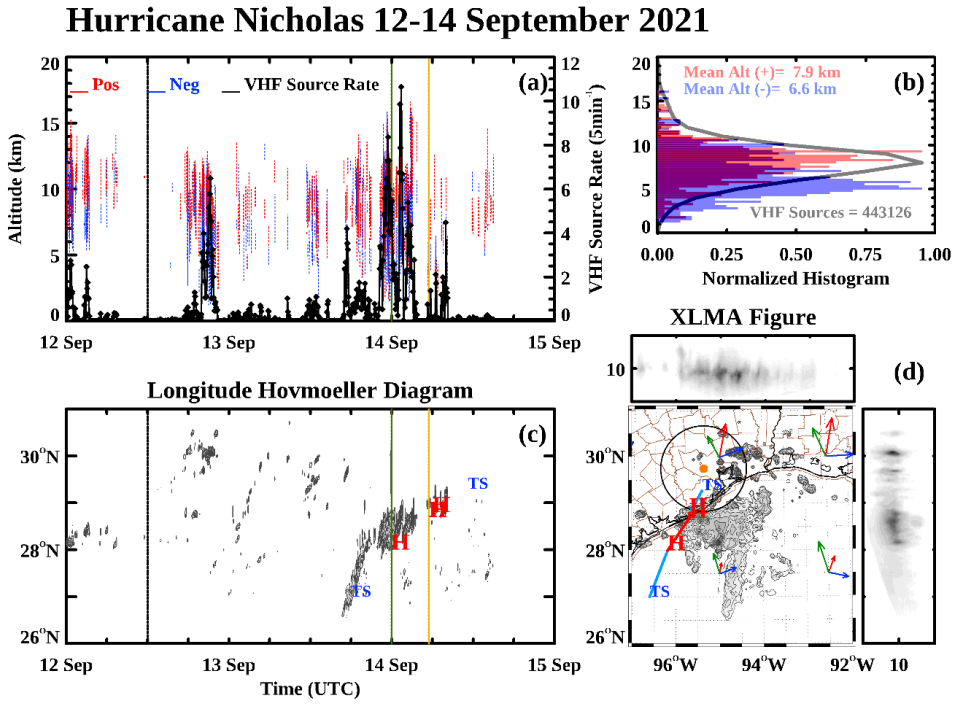

Figure 1. (a) VHF source rate (in thousands) and ChargePol charge region polarity. Tropical storm status indicated by black line, green line (hurricane status), and gold line (landfall). (b) Most probable height of VHF sources (gray line) and mean heights of the overall VHF sources (gray line) along with positive (red) and negative (blue) charge regions. (c) Hovmoeller diagram of VHF source density. The relative times of tropical storm (TS) and hurricane (H) status are shown at the respective latitude of the center of circulation. (d) "XLMA" style figure showing overall VHF source density (plan view), longitude-altitude (top box) and latitude-altitude (right box). Black circle indicates 100 km radius from HLMA centroid. The NHC storm track is overlain. The NCEP/NCAR (Kalnay et al., 1996) low-level shear (red arrows), deep layer shear (blue vectors), and mean 850 hPa winds (green vectors) are provided for the 12-14 September 2021 period.

Figure 1 shows the VHF source rate, charge region heights, spatiotemporal VHF source density, and charge analysis during the entire life cycle of Nicholas from 12-14 September 2021. A total of 443,126 sources were identified by the HLMA. After 1700 UTC on 13 September, rainband lightning activity intensified and lasted until Tropical Storm Nicholas (blue TS) was upgraded to a Category 1 hurricane (red H and green line) with the center of circulation approaching 28°N (Figures 1c and 1d). Rainband lightning activity began to wane as lightning activity within the eyewall became more prominent after 0000 UTC 14 September 2021. At 0100 UTC, the VHF source rate increased to the highest values of the entire event (10,642 sources (5 $min)^{-1}$) (Figures 1a and 1c). There was a decline in lightning activity after 0230 UTC and a final round of weak electrified convection developed as Nicholas officially made landfall at 0530 UTC (gold line).

Figure 1b presents a depiction of the height distribution of VHF sources normalized to the maximum value of sources (gray line). The -40°C isotherm level is generally associated with instantaneous freezing (e.g., glaciation) of all supercooled water droplets within a cloud and corresponds to an altitude of 9-10 km AGL. This explains the typical altitude where the positive charge layer is identified by LMAs. According to the LCH and CRP soundings from 1200 UTC 12 September to 1200 UTC 14 September, the environmental temperature at that altitude range was closer to -30°C. The overall most probable height of the VHF sources during Nicholas was roughly 8 km, which corresponded to a temperature of -18°C. Because Nicholas is a tropical system, warm air parcels are advected by the wind motion which acts to increase the thickness between pressure/temperature surfaces with respect to height. Note that a small contribution of upper-level VHF sources was apparent by the upper "tail" of the altitude distribution above 15 km.

A detailed discussion of the charge analysis (positive and negative regions) with respect to Nicholas' intensification is presented in section 4.

Figure 1d indicated that the low-level and deep layer wind shear favored electrified convection north and east of the center of circulation during a three-day period. The southerly low-level and southwesterly deep layer shear vectors in the vicinity of the center of Nicholas were at a 45^{o} angle for nearly the entire TC event. Though wind shear is generally disruptive to hurricane intensification, the northeastward movement of Nicholas in line with the wind shear likely favored the sustaining of intense convection observed in both the rainband and eyewall regions (Latto & Berg, 2022).

3.3 Rainband and Eyewall

Figures 2 and 3 illustrate only the VHF sources from Nicholas' rainband and eyewall, respectively (i.e., sources from other convection were removed by XLMA). Much of the electrified convection was confined to the regions north and east of the center of circulation for the eyewall and rainband cases. VHF source rates initially peaked at roughly 1,000 sources (5 min)$^{-1}$ from 1700-2000 UTC on 13 September resulting from weak rainband convective activity that propagated northward over time (Figures 2a and 2c). As the source rate declined, an apparent megaflash occurred in the outer rainband region at 2004 UTC (Figures 2c and 2d). The VHF source rate increased substantially to around 5,000 sources (5 min)$^{-1}$ during the period from 2200-2300 UTC as the strongest convective cells within the rainband developed. Rainband lightning activity began to diminish after 0000 UTC on 14 September. There was a secondary increase in VHF source rate (~3,500 sources (5 min)$^{-1}$) at 0200 UTC resulting from additional development of deep convective cells located in the northeast region of the rainband (Figures 2c and 2d).

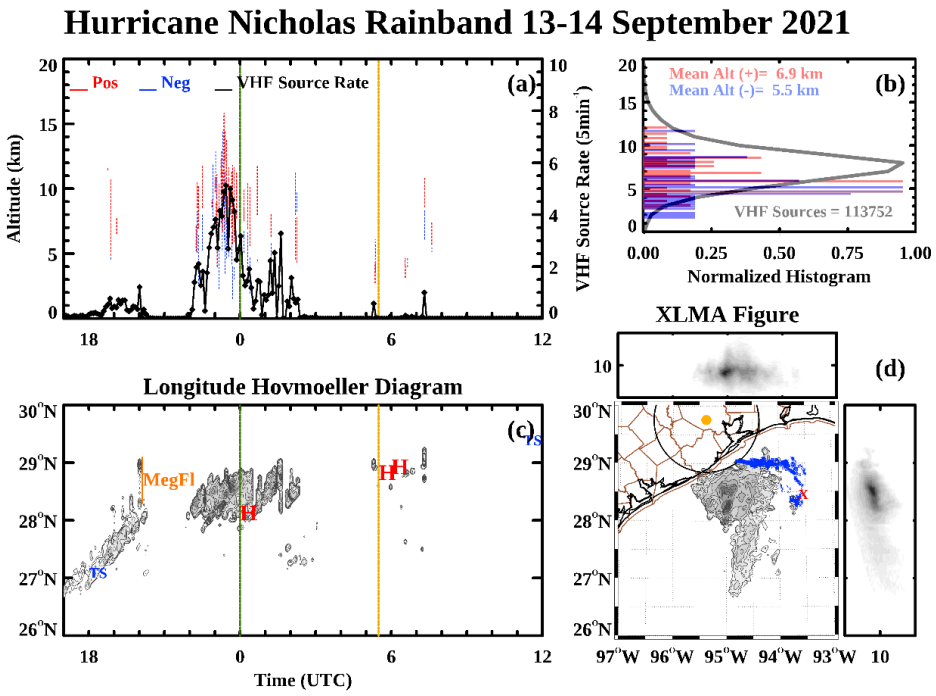

Figure 2. Same as Figure 1 but for the rainband VHF sources only from 1700 UTC 13 September 2021 to 1200 UTC 14 September 2021. The megaflash (MegFL) is included in (c) and the VHF source points of the megaflash are overlain in (d). The initiation point of the 2004 UTC 13 September 2021 megaflash case is denoted by the red "X".

There were two distinct bursts of eyewall lightning. The first occurred in the eastern eyewall region with the second occurring in the western eyewall region (Figure 3a). Figure 3c showed that as Nicholas propagated northward, there was weak electrical activity until 0100 UTC on 14 September. The VHF source rate was nearly 5,600 sources $(5\ min)^{-1}$ at the peak of the lightning activity (0130 UTC). At 0200 UTC, the convection migrated northward and westward around the eyewall and re-intensified yielding a VHF source rate of ~4,500 sources $(5\ min)^{-1}$ at 0230 UTC. A few TLEs were observed by the HLMA between 0230-0300 UTC as lightning activity declined. The last round of weak lightning activity occurred after 0530 UTC with source rates diminishing to less than 1,500 sources $(5\ min)^{-1}$, indicating fewer electrified convective cells and rapid weakening of the tropical cyclone underway (e.g., rise in central pressure). Note that the

rainband (26%) and eyewall (16%) sources made up a combined 42% of the lightning activity during Nicholas.

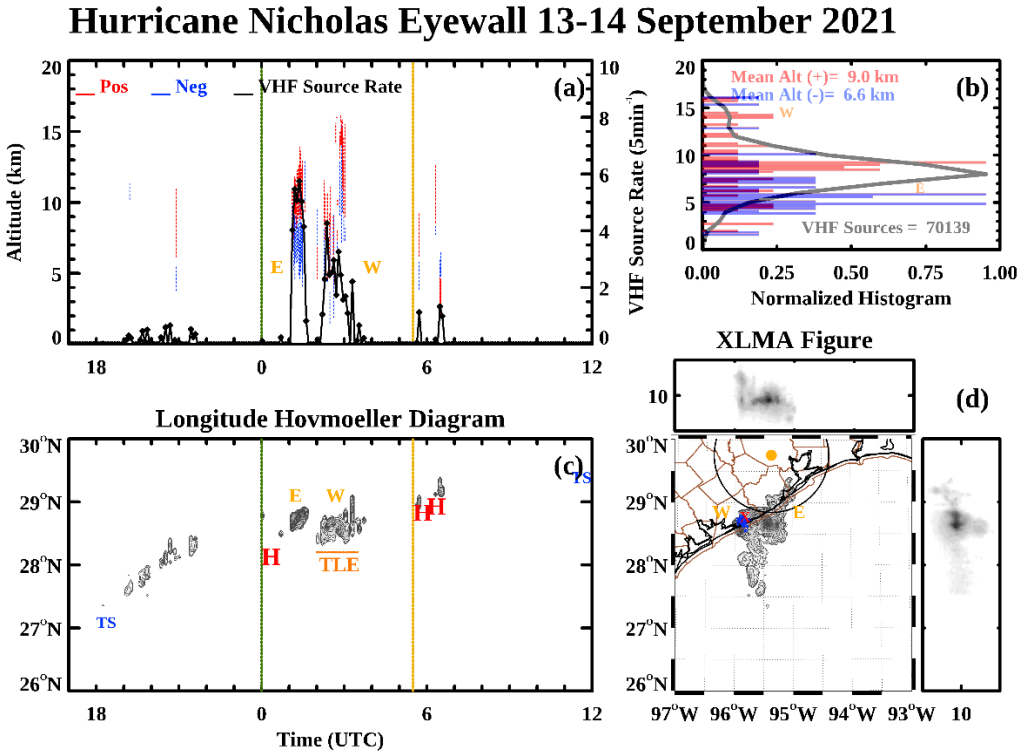

Figure 3. Same as Figure 2 but for the eyewall VHF sources only. The TLE cases are included in (c) and the VHF source points of the TLE cases are overlain in (d). The initiation point of the 0230-0240 UTC 14 September 2021 cases is denoted by the red "X". "E" and "W" highlight eastern and western eyewall electrified cellular convection.

Though the most probable heights of the eyewall and rainband lightning were similar (8 km), there was a higher frequency of sources above 15 km in the western eyewall region than the eastern eyewall and rainband regions (Figures 2b and 3b). Additionally, two features were apparent: (i) an increase in the rate of VHF sources in the rainband preceded the upgrade of Nicholas to hurricane status and (ii) the highest VHF source rates occurred in the eyewall region after Nicholas became a hurricane. The relative contributions of the rainband and eyewall electrification to the overall charge structure of Nicholas are discussed further in section 4.

335 3.4 Megaflash and TLEs

Figures 4-8 depict the spatiotemporal nature electrical activity of the megaflash and TLE cases along with corresponding GridRad plan and cross-section reflectivity scans encompassing the approximate case times. In addition, all cases have been animated and their respective charge layers were manually analyzed using XLMA. The animations are provided as Supplemental
340 Figures 1-5. A brief description of the charge analysis is presented in the following subsections.

3.4.1 Megaflash Case

Figure 4 featured a curved megaflash at approximately 20:04:56 UTC on 13 September 2021 (Figure 4a). The initial VHF source point was located at 6 km and lasted for nearly 1.6 s. The megaflash was initially associated with a negative intracloud stroke. Two more negative intracloud
345 strokes followed and the last recorded intracloud stroke was positive. Of the five ground flashes, the first two were denoted by the two positive peak current strokes of 94 and 161 kA. The next two ground strokes were also positive while the final stroke was negative.

In Figures 4b and 4c, most of the positive VHF source points were located between the melting level and the -10^{o}C isotherm (6 km) while negative VHF source points were concentrated
350 at ~8-9 km in a colder region (< -20^{o}C). The negative intracloud and strong positive ground strokes at the time of the megaflash indicate the presence of an inverted charge structure. There was a small negative charge layer underlying the positive layer, which suggests an inverted dipole with some evidence of an inverted tripole. Figures 4b and 4e show that the VHF source points comprising the megaflash were located in the stratiform region of the outer rainband convection.
355 In addition, the radar reflectivity was less than 35 dBZ in the vicinity of the source points. Note that there was weak reflectivity, and no source points were observed above the glaciated level (-

40°C). Figure 4d shows that the VHF source points exhibited a bidirectional propagation away from the initial point. When animated by XLMA (Supplemental Figure 1), a small pocket of sources (black/blue symbols) first appeared south of the white "X" (28.5°N, 93.4°W) with the northern and western source points (e.g., blue, purple, green, orange, and red symbols) appearing after. Furthermore, the megaflash traveled a straightened distance of nearly 220 km.

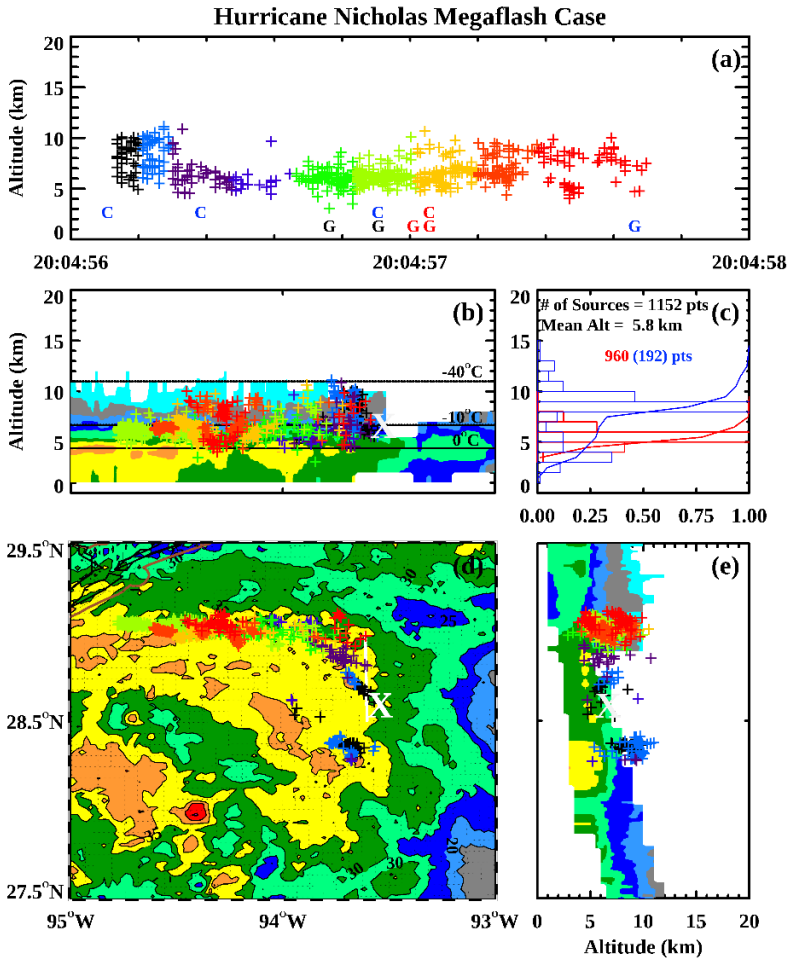

Figure 4. "XLMA" style figure showing (a) Progression of VHF sources color coded by time, NLDN intracloud (C) and ground (G) strokes color coded by polarity, (b) Longitude-altitude plot of VHF sources and GridRad reflectivity along with the environmental temperatures from the LCH, (c) VHF source distribution, mean altitude, and polarity of the charge layers, and cumulative density of positive (red line) and negative (blue line) sources, (d) GridRad plan view with overlain VHF sources. Cross-section latitude and longitude are denoted by white lines and initial point of flash is denoted by white "X", (e) Latitude-altitude plot of (b).

370 3.4.2 TLE Cases

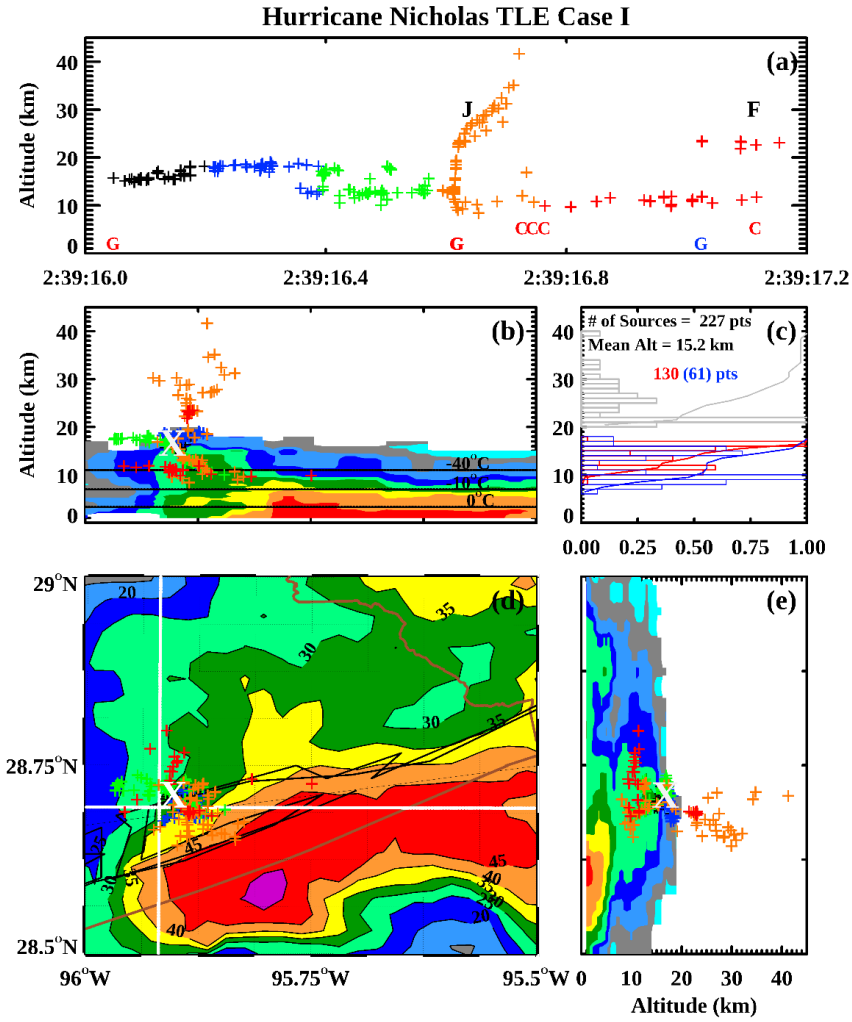

Figure 5. Same as Figure 4 but for TLE Case I. "J" denotes a possible jet TLE while "F" denotes a failed "bolt from the blue" (BFB). Note that altitude is adjusted to include VHF sources beyond 20 km (gray) and no cumulative density is plotted for those sources.

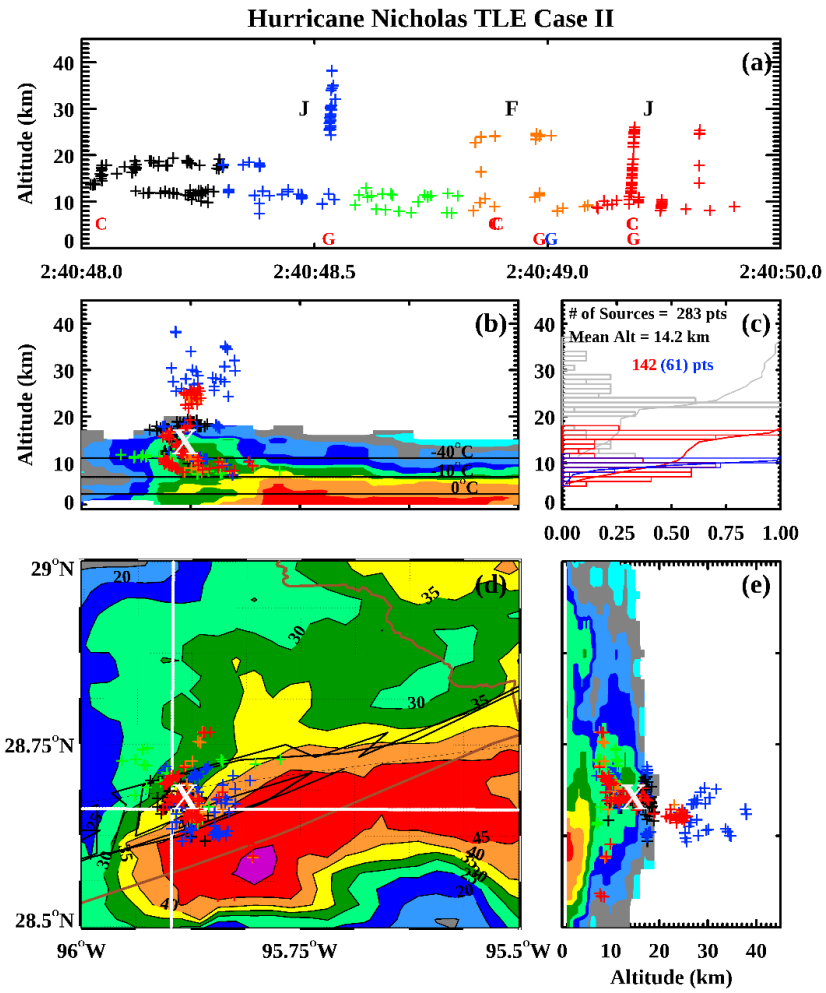

375

Figure 6. Same as Figure 4 but for TLE Case II

Case I featured a lightning flash exhibiting "jet-like" characteristics ("J") at approximately 02:39:16 UTC on 14 September 2021 (Figure 5a). The initial VHF source point appeared at 14 km and the flash lasted for nearly 1.2 s. The actual jet occurred at around 02:39:16.6 UTC and reached
380 a maximum altitude of 40 km. A few failed "bolt-from-the-blue (BFB)" discharges ("F") (e.g., Lu et al., 2011) followed the jet at approximately 02:39:17.0 UTC. Failed BFBs are denoted by VHF source points having an inverted "L" shape configuration which can precede or follow a jet. Note that when animated, the jet reached a maximum altitude of 40 km nearly 700 ms into the flash (Supplemental Figure 2). There were four ground strokes with the first one of positive polarity

occurring at the time of the initial VHF source. Two positive ground strokes followed and were observed at the same time as the jet. Note that both strokes occurred within microseconds of one another and appear as one stroke at 02:39:16.7 UTC. The final ground flash was observed during the period of failed BFBs and was negative. Four positive intracloud strokes were observed after the jet with the final intracloud stroke occurring during the period of the failed BFBs.

In Figures 5b and 5c, most of the positive VHF source points were located well above the glaciated level (-40^{o}C isotherm at 11 km) at ~17 km. The negative VHF source points peaked between 9-10 km (-30^{o}C). However, there was one notable negative charge layer at 15 km and a small screening layer at 19 km. The 0240 UTC radar scan indicated that the 30 dBZ reflectivity echo height exceeded 15 km in the vicinity of the initial flash source point (Figures 5b and 5e). Figure 5d shows that the TLE occurred within the northwest periphery of an intense deep convective core in the western eyewall region (> 50 dBZ). It was evident that the cell featured an overall inverted dipole with hints of additional complex charge structures. Moreover, the reflectivity orientation shown in the cross-sections (Figures 5b and 5e) suggested a highly sheared environment where the jet formed. The plume of VHF sources was depicted as an eastward leaning cone in Figure 5b and was oriented to the south in Figure 5e. This was likely related to the counterclockwise motion of deep convective cells around the eyewall (Figure 5d).

Case II occurred over a minute later (02:40:48 UTC) and lasted for roughly 2 s. The initial VHF source point of the flash was located at 12 km and featured two jets (Figure 6a). The first jet occurred nearly 500 ms after the initial VHF source and reached a maximum altitude of 36.5 km. The second jet occurred at 02:40:49.4 UTC, or 1.4 seconds into the event and reached a maximum altitude of 24 km. Note that a third jet may have also occurred at 02:40:49.7 UTC but the lack of source points at that time makes this claim uncertain. Failed BFBs were observed nearly 300 ms

after the first jet and 500 ms before the second jet. There were four ground strokes with the first one of positive polarity occurring at the time of the first jet. A positive and negative ground stroke were observed during the period of the BFBs while the final ground flash was observed during the second jet. Four intracloud strokes were observed with the first one occurring at the beginning of the flash. Two more occurred during the BFB period and the final occurred at the same time as the final ground stroke. Similar to Case I, all intracloud strokes were positive. Note that Case I and Case II share the same radar volume scan.

In Figures 6b and 6c, most of the positive VHF source points were above 11 km. The negative VHF source points peaked at 10 km. There was a notable positive screening layer at 19 km in contrast to Case I. However, Case II also featured an overall inverted tripole structure due to a small positive charge region (7 km) underlying the robust negative charge region. Figure 6d shows a more concentrated plume of VHF sources northwest of the convective core. In contrast to Case I, the plume of VHF source points exhibited a weaker orientation to the south and east (i.e., the source points were oriented straight upwards). The animation of Case II (Supplemental Figure 3) illustrated the first jet providing a channel in which the second jet followed with some evidence of VHF sources from the third jet.

The Case III flash lasted for nearly 2.5 s (Figure 7a). Case III featured two jets at 02:50:52.6 and 02:50:53.4 UTC along with a possible third jet just after 02:50:53.5 UTC. It is not entirely evident that the first jet was continuous because (a) it terminated at an altitude of 21 km and (b) VHF sources approaching 42 km were observed nearly 200 ms after the initial appearance of the jet. The second jet featured VHF sources reaching an altitude of 26 km. The initial VHF source altitude was 12.9 km with no corresponding lightning strokes. There were no discernible failed BFBs during the flash. There were three ground strokes having positive polarity with the third one

occurring at the time of the first jet. There were six intracloud strokes with the third one occurring with the uppermost VHF sources. No strokes were associated with the subsequent jets. This is not to say that there was no observable lightning, but that the NLDN was not able to capture any ground or intracloud strokes at that time (Cummins et al., 2009; Liu et al., 2015).

Figures 7b and 7c revealed VHF source points primarily clustered at or below the glaciated level. There was an extensive upper charge region peaking at 15 km populated by a mixture of negative and positive VHF sources with an underlying robust positive charge region at 8 km. There was a slight negative screening layer at 19 km. This case exhibited an inverted dipole charge structure. The 0250 UTC radar scan happened nearly 10 minutes after Cases I and II and showed a shrinking of the convective core (Figure 7d). Figure 7d shows widely scattered VHF sources now southwest of the convective core. The apparent southward and westward tilt of the cone-like projection of VHF sources, downshear of the convective core, was also evident in the animation (see Supplemental Figure 4) and in Figures 7b and 7e. The cone-like projection of the plume of VHF sources is nearly vertical in Figure 7e.

The Case IV flash initiated at 14.2 km and lasted for 1.4 s. The flash featured a barely discernible first jet just after 02:51:49.6 UTC and a second jet at 02:51:50.15 UTC following two observed failed BFBs at 02:51:49.25 UTC and 02:51:49.35 UTC (Figure 8a). Note that the second jet occurred at the end of the flash. The VHF sources of the first and second jets reached 24.6 and 26.4 km in altitude respectively and represented the lowest maximum altitudes of all the TLE cases. The first and second jets also exhibited different orientations during their development (Supplemental Figure 5).

Figures 8b and 8c showed VHF source points clustered above the glaciated level similar to Cases I and II. There was a notable upper negative charge region peaking at 17 km with an

underlying deep positive charge region extending from 10-16 km. The upper screening layer from 19-20 km was robust and negative. This case was similar to the previous three cases by featuring an overall inverted dipole charge structure. The 0255 UTC radar scan showed a re-intensification of the convective core which was the largest of all the cases (Figure 8d). The VHF sources were oriented westward of the convective core in Figure 8d, but the VHF sources in the jet were oriented to east and south (Figures 8b and 8e). Note that Figure 8e does reveal a cone-like configuration of VHF source points as in the previous cases. Moreover, the location of the initial point was the most southeastwardly displaced indicating the cyclonic motion of the eyewall deep convection (Figure 8d).

Case IV displayed prolific intracloud and ground strokes. There were seven intracloud and nine ground strokes which led all cases for the total number of strokes. The second intracloud stroke was negative and all other strokes were positive. The final two intracloud strokes occurred at the times of the two jets. One possible explanation is that the shear amount of lightning could have acted to discharge the flash channel enough to reduce the maximum altitude of the jets. It is apparent that the maximum altitude of the megaflash and TLE cases depended on factors such as VHF source distribution with respect to the melting and glaciation levels, charge layer polarity and altitude, and mode of convection. The dynamic factors responsible for the electrical nature of the cases are detailed in the next section.

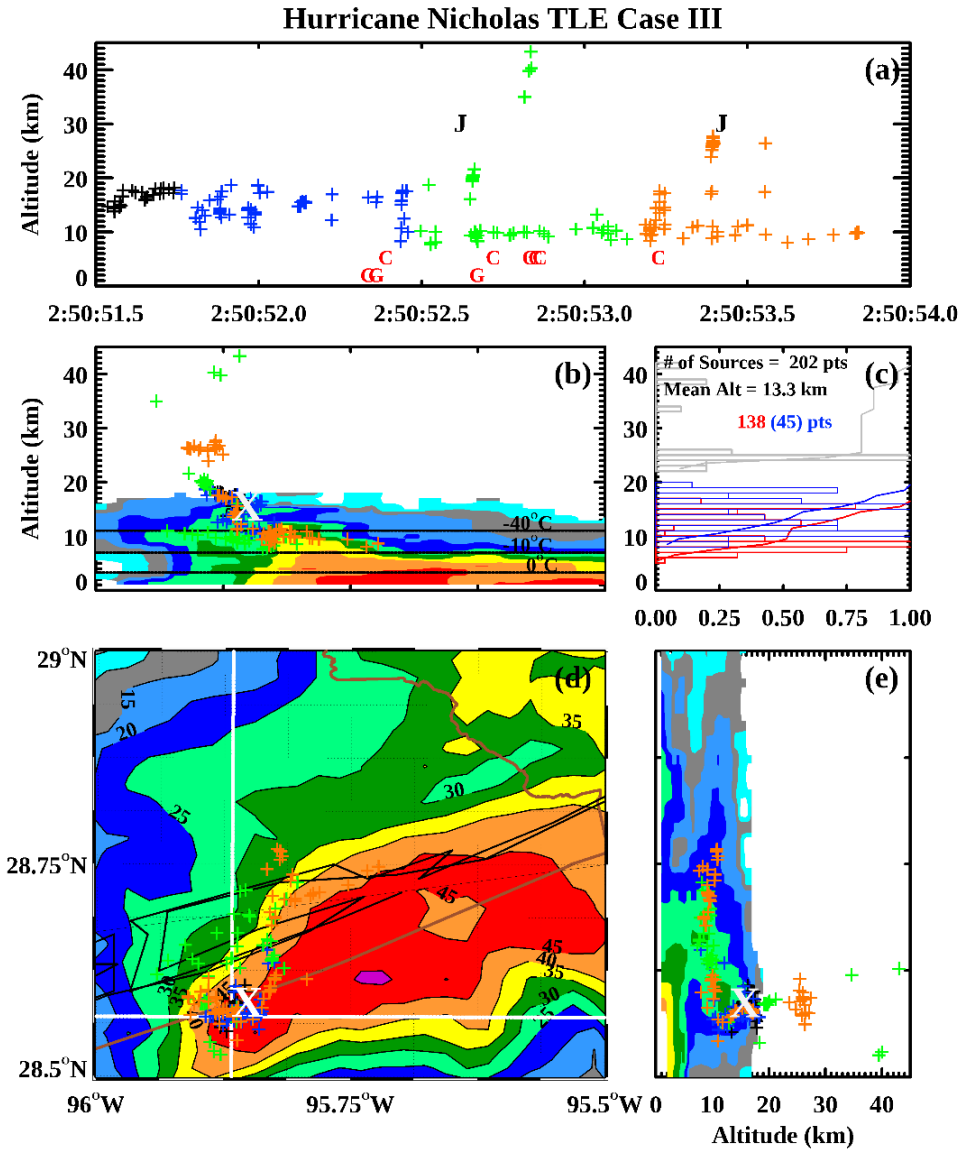

Figure 7. Same as Figure 4 but for TLE Case III

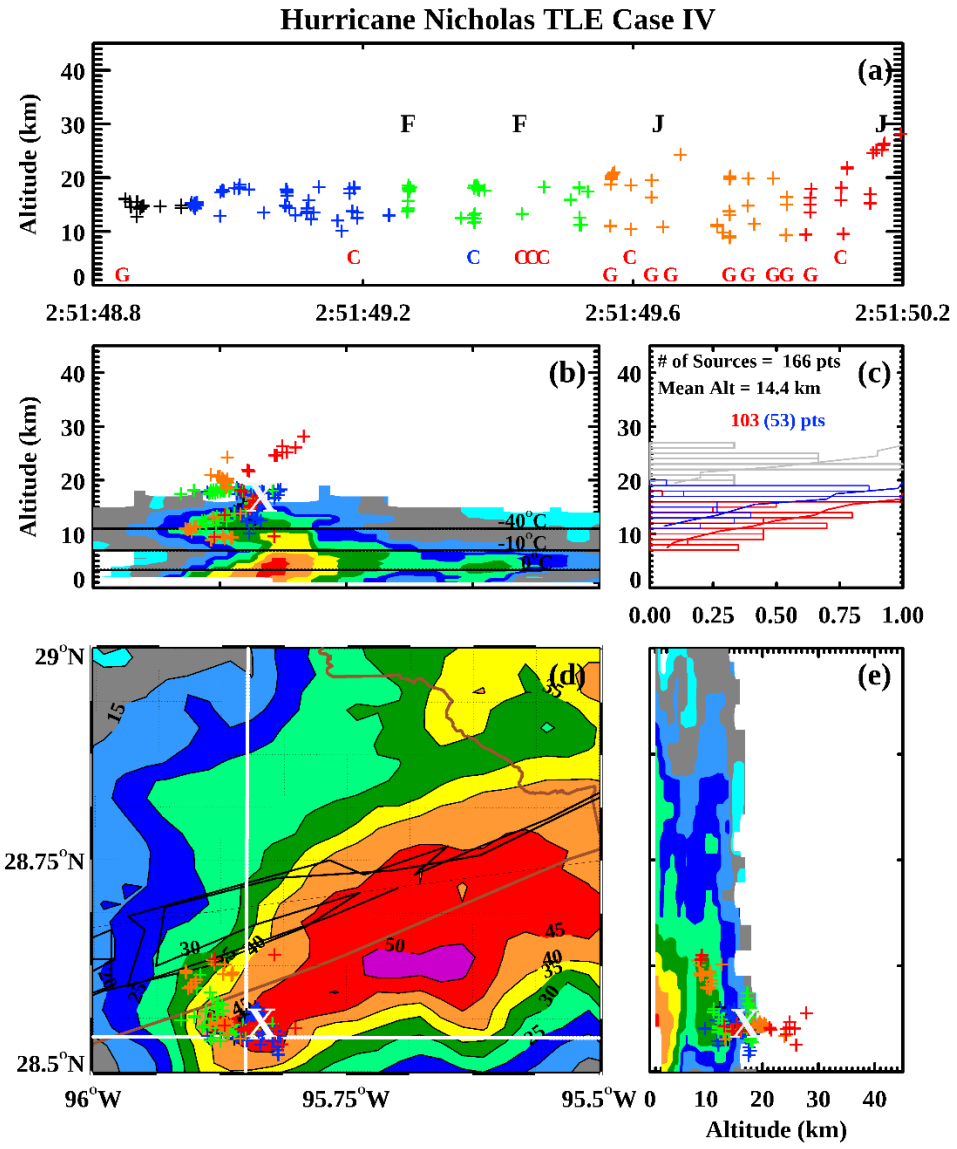

Figure 8. Same as Figure 4 but for TLE Case IV

480

4. Discussion of rainband and eyewall lightning events

4.1 Meteorological conditions for the rainband and eyewall

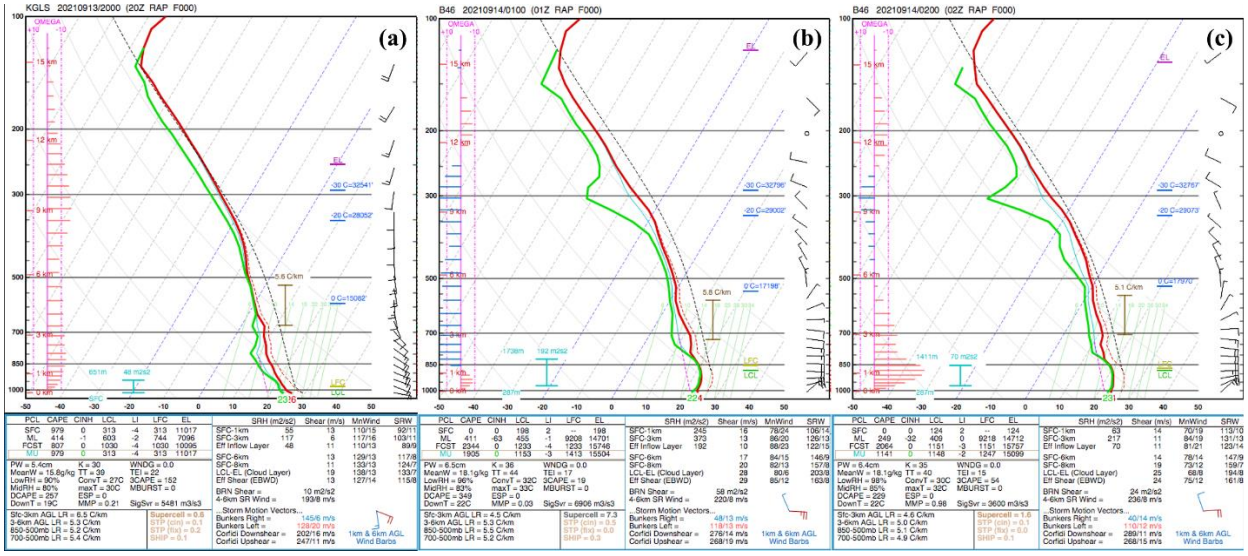

Figure 9. RAP forecast soundings initialized at 2000 UTC (13 September 2021), (b) 0100 UTC (14 September 2021), and (c) 0200 UTC (14 September 2021). The soundings were produced by SharpPy (Blumberg et al., 2017).

The RAP forecast sounding from 2000 UTC 13 September, taken from a grid point near Galveston (29.3°N, 94.9°W), was used to illustrate the dynamic and thermodynamic environment of the rainband during the megaflash case (Figure 9a). The surface convective available potential energy (CAPE) was 979 J kg^{-1}. In addition, the effective storm-relative helicity (SRH) was 48 m^2 s^{-2} and the surface-3 km SRH was 117 m^2 s^{-2}. The wind vectors veered from southeasterly to southerly with height from the surface up to around 9 km. The low-level (surface to 1 km) and deep layer (surface to 8 km) wind shear values were 13 and 11 m s^{-1}, respectively. Furthermore, the depth of the atmosphere was at or near saturation indicating robust moist conditions. The CAPE values indicate updrafts capable of supporting electrified convection while the SRH values suggested possible multicellular convection with some embedded rotating cells.

Due to the veering low- to mid-level wind profile, it is possible that a broad charge layer developed from turbulent deep convection near the eyewall and expanded northeastward due to upper-level winds that were out of the southwest (Figure 9a). Over time, the charge layer was advected downward through gravitational settling as shown by the abundance of VHF sources near the melting layer (Figures 4b and 4e). In addition, the expansiveness of the charge layer may have been enhanced by secondary ice particles formed by collisions due to turbulence at or just above the melting layer (e.g., Hallet-Mossop and ice splintering processes) (Black and Hallett 1986; Fierro and Mansell 2017; Hallett and Mossop 1974; Qu et al., 2022; Peterson, 2023). The complex cyclonic wind motion and shear interaction in the outer rainband may have acted to warp the low-level charge region in which the megaflash initiated. That is, the discharge had to follow the orientation of the electric field.

For the eyewall and TLE cases, the RAP 0100 UTC and 0200 UTC 14 September soundings were taken from a grid point (28.3^{o}N, 95.6^{o}W) located near the eyewall (Figures 9b and 9c). These times corresponded to the peak VHF source rates observed at 0130 and 0230 UTC. Surface CAPE values were zero for both soundings, effective SRH values were 192 and 70 m^2 s^{-2}, and wind vectors backed northwesterly between 6-11 km AGL for the respective 0100 and 0200 UTC soundings. Low-level and deep layer shear for the 0100 (0200) UTC cases were 16 (14) and 20 (19) m s^{-1}, respectively. Note that deep convection was prevalent despite no presence of surface CAPE. Hence, most unstable CAPE (MUCAPE), a measure of overall buoyancy of air parcels above the surface, is used to explain the nature of the elevated deep convection for the TLE cases. MUCAPE values were 1905 and 1141 m^2 s^{-2}, for the respective 0100 and 0200 UTC RAP soundings. MUCAPE, SRH, and wind shear magnitudes indicate an environment conducive to non-surface based electrified convection.

Moreover, the upper-level northwesterly wind vectors in the RAP soundings also help to explain the orientation of deep convection and location of the TLEs. There was a prominent southeastward displacement of the white "X" and plume of VHF sources shown in Figures 5-8. The CAPE and SRH values progressively decreased for subsequent hourly RAP soundings after 0300 UTC (not shown), indicating that the environment was becoming less favorable for intensification and electrification. This was consistent with the official NHC advisories for Nicholas because although the maximum sustained winds increased modestly between the 0000 and 0300 UTC advisories, the minimum central pressure remained steady.

Figure 10 shows a brief progression of strong upper-level divergence developing in the western eyewall region between 0240-0255 UTC on 14 September. The divergence removed air from the cloud top helping to increase updraft strength. The divergence was collocated with radar echo top heights exceeding 15 km supporting the occurrence of vigorous convection and high-altitude lightning activity in the western eyewall region. Wind vectors backing with height generally implies dry air intrusion (Figures 9b and 9c). Shu et al. (2021) pointed out that this may be an additional reason the upper-level divergence and deep convection strengthened and produced the TLEs. A strong downdraft upshear (northeast) of the TLE producing cell (white "X"), caused by divergent outflow, was likely responsible for a 42 m s^{-1} (82 kt) surface wind gust recorded by emergency responders (personal communication) and coastal surface observation stations around 0240 UTC (Latto & Berg, 2022). Note that this was also around the time of the second maximum in VHF source rate (see Figure 3) and lends further support to a possible second brief intensification of Nicholas.

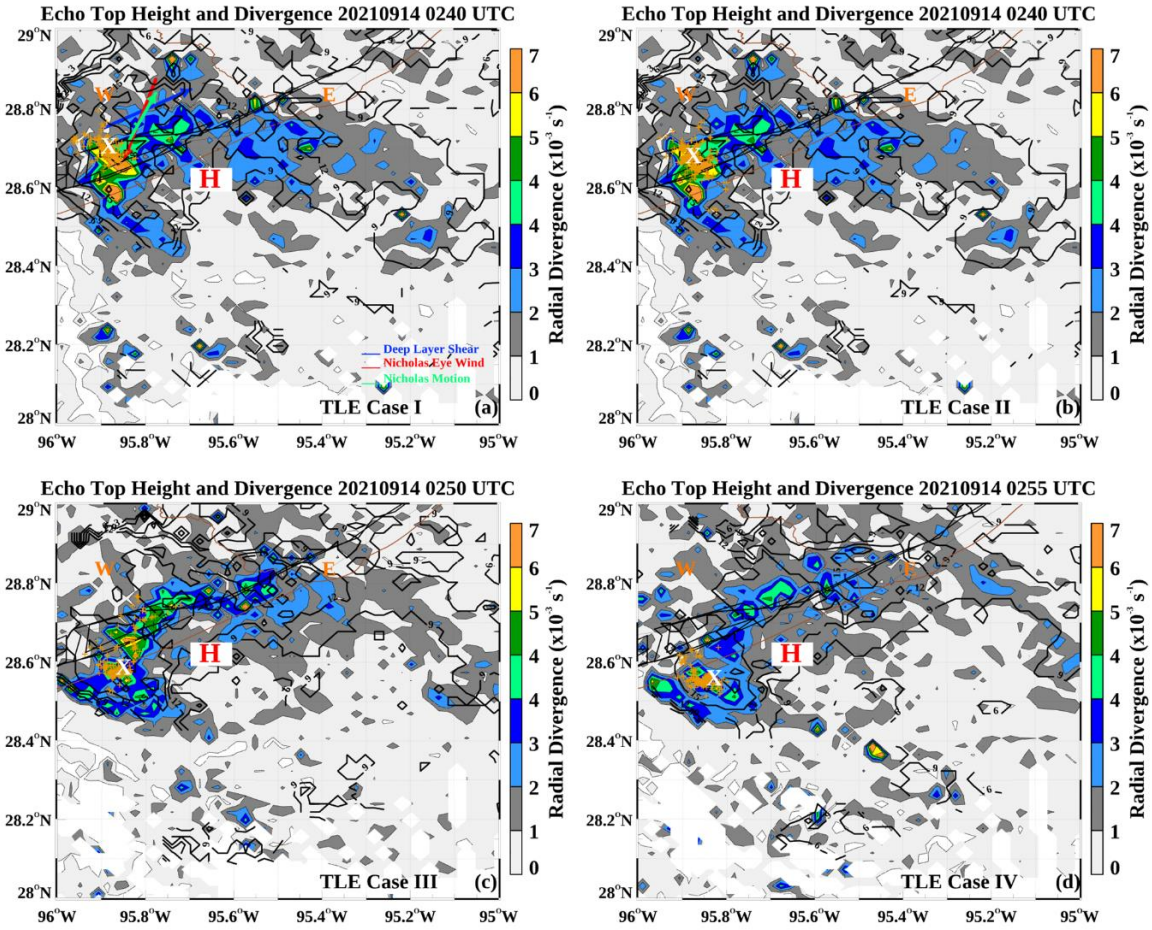

Figure 10. NEXRAD derived cloud top height (black line contours denote altitude in kilometers) and divergence (color filled contours) during TLE Cases I-IV (a-d). VHF sources are denoted by gold pluses and initiation point by white "X". Estimated deep-layer, convective cell, and direction vectors of Nicholas during Case I are used to help explain the intensification of the TLE-producing deep convection (e.g., Wadler et al., 2022) in (a). Interpolated center of Nicholas (28.6°N, 95.7°W) during this time is denoted by red "H". Animated version is presented in Supplemental Movie 2.

The megaflash was located in the "warm and moist side" in the rainband region (e.g., Figure 9a) while vigorous TLE convection was located in the "cool and dry side" of the western eyewall region (e.g., Figures 9b and 9c) according to Wadler et al. (2022). Moreover, an additional compensating effect may have been in action according to Shu et al. (2021). Eventually, continued dry air intrusion can modulate the vertical precipitation structure and eventually expand the stratiform region thereby weakening the overall convection. This in fact did occur after 0300 UTC

when lightning and TLE activity had virtually ended in the rainband and eyewall (Supplemental Movies 1 and 2). This is also supported by Wadler et al. (2022) who pointed out that southerly deep-layer shear orientation generates asymmetry in TCs and less favorable conditions for surface-based convection.

4.2 Charge analysis of the rainband and eyewall

ChargePol and XLMA analysis revealed a mean positive (negative) charge layer height of 7.9 km (6.6 km) was close to the most probable VHF source height value of 8 km (Figure 1c). Overall, Nicholas featured a "normal" dipole charge structure with a mixture of inverted dipole and tripole structures. That is, there was a large region of negative charge at 5 km and a small region of negative charge at 10 km which "sandwiched" the dominant positive charge region (9 km) (Figures 1a and 1b). The upper "tail" of the distribution clearly shows the contribution of high-altitude sources from the rainband and eyewall convection.

At 1900 UTC on 13 September, a robust positive charge region in the rainband developed prior to the megaflash (Figures 2a and 2b). Due to the distance away from the HLMA centroid, ChargePol could resolve a partial entire spatial and temporal charge structure of the megaflash (2004 UTC). ChargePol did indicate a developing charge inversion given the lower initial altitude and deep depth of the positive charge region. At 2330 UTC, the positive charge layer ascended to ~15 km indicating the strengthening of the deep convection along the 95^{o}W meridian extending from a latitude of 28^{o}N up to 28.5^{o}N (Figures 2c and 2d). After Nicholas made landfall there was a return to predominantly normal charge structures as the lightning activity declined (Figure 2a).

The eastern eyewall convection from 0100-0200 UTC on 14 September exhibited a normal dipole and was the dominant contributor to the charge time series and histogram distribution (Figures 3a and 3b). The western eyewall region featured an inverted dipole primarily during the

period from 0200-0300 UTC. A low-level negative charge region developed ahead of the upper-level positive charge region at 0230 UTC during the second maximum of VHF source rates (Figure 3a). Moreover, a thin negative charge layer was observed above the positive charge layer at 16 km (Figure 3b). Cases I, III, and IV had the largest contributions of negative VHF sources at that level, while Case II featured a higher number of positive VHF sources. After Nicholas made landfall, eyewall charge structure information was somewhat ambiguous.

ChargePol yielded reasonable results regarding charge structures of the tropical deep convection during Nicholas. However, the polarity of the TLEs was not well established because the positive and negative charge regions from 16 km and downward were primarily resolved by ChargePol. The contribution of VHF sources above 16 km were fewer in comparison and ChargePol is not currently designed to identify the polarity of charge regions above 20 km. Future work will involve using ChargePol in conjunction with manual XLMA charge analysis and incorporating charge moment change and magnetic field analysis to quantify the charge transfer of TLEs to the upper atmosphere during tropical and continental deep convective events in the vicinity of the HLMA.

5. Summary

Hurricane Nicholas made landfall along the Texas Gulf Coast at 0530 UTC on 14 September 2021. The Houston Lightning Mapping Array (HLMA) was operational and captured nearly all the lightning activity of Nicholas from 12-14 September 2021. There was appreciable deep convection observed during the TC and several notable features were observed prior to landfall. Rainband lightning activity sharply increased two hours before Nicholas rapidly intensified to a Category 1 hurricane at 0000 UTC 14 September 2021. Between 0100-0300 UTC, eyewall lightning activity became more dominant. By the time Nicholas made landfall, rainband

and eyewall deep convection was minimal. Rare lightning events during the TC were observed by the HLMA: (a) an apparent megaflash (linear distance of 220 km) occurred at 2004 UTC on 13 September 2021 in the outermost rainband and appeared to be curved and (b) several jet-like TLEs occurred between 0230-0300 UTC on 14 September 2021 in the western eyewall region. Moreover, at around the time of the first observable TLE (0238 UTC), a surface wind gust of 42 m s^{-1} (82 kt) was reported.

Rainband and eyewall lightning activity differed in rate, altitude, and charge structure. The rainband (eyewall) had 26% (16%) of all VHF sources during Nicholas. There was a sharp increase in rainband VHF source rate prior to Nicholas being upgraded to a Category 1 TC. On the other hand, the VHF source rate was higher in the eyewall along with the mean height of the positive charge region (9 km) compared to the rainband (7 km). This indicates that deep convection was more widespread within the rainband, while the eyewall deep convective cells were more localized and vigorous. The charge structure of Nicholas featured a predominantly normal structure (positive charge region overlying negative charge) with instances of inverted charge (negative charge region overlying a positive region) especially within the eyewall. A low-level (5-7 km) charge inversion was present during the time of the megaflash while an upper-level (15-18 km) charge inversion occurred during the time of the several TLEs.

The dynamic environment was not only favorable for the rapid intensification of Nicholas but also the observations of the rare lightning events. Southwesterly low-level and westerly deep layer wind shear vector orientation (~45^{o}) along with the northeastward movement of Nicholas favored electrified deep convection north and east of the center of circulation. Two hours prior to Nicholas being upgraded to a hurricane (2000 UTC 13 September 2021), an expansive region of low-level charge developed in the outer rainband region where the megaflash initiated. The curved

nature of the megaflash resulted from the complex interaction between the cyclonic wind motion and turbulence (e.g., low-level veering wind profile) warping the low-level charge layer. During the period of 0230-0300 UTC (14 September 2021), additional dynamic enhancements such as backing of upper-level winds with height and upper-level divergence within the western region of the eyewall likely facilitated the conditions needed to erode the upper-level screening charge layer and produce the TLEs.

The small-scale spatial and temporal resolution of the HLMA identified several features within the electrified tropical convection of Nicholas that may have been overlooked by other surface-, aircraft-, and space-based measurement platforms. Hence, lightning mapping arrays are useful tools in analyzing and discerning the electrified nature of TCs which develop and evolve within their confines. In addition, since ChargePol can output reasonable charge structure data in 4-D, it will be modified and enhanced in future work to examine the spatial and temporal charge structure of electrified deep convection in continental and tropical systems.

Acknowledgements

This study combines the results of thesis work performed by Jacob Hale and Sydney Butler. The authors are grateful for the help of Eric Bruning (personal communication and lmatools software package support), Bruno Medina and Lawrence Carey (ChargePol software package support), and Levi Boggs (personal communication for jets and TLEs). The authors are grateful to Edward Lightbourn for providing ground validation measurements. The NLDN data were provided by Vaisala, Inc and were requested via their educational data service. NOAA/NCEP wind shear and mean wind data were provided by the NOAA PSL, Boulder, Colorado, USA, from their website at https://psl.noaa.gov. This study is supported in part by the National Science Foundation (Grant AGS-2019858).

Conflict of Interest

The authors declare no conflicts of interest relevant to this study.

Data Availability Statement

Houston Lightning Mapping Array sensor data are curated and processed by Timothy Logan. The data are available in the Texas Data Repository at https://doi.org/10.18738/T8/6IG8T1. “lmatools” source code is available at https://github.com/deeplycloudy/lmatools. ChargePol source code is available at https://github.com/brmedin/chargepol. GridRad NEXRAD products are available at https://gridrad.org. RAP soundings are provided by SharpPy, and the source code is available at https://github.com/sharppy/SHARPpy.

References

Black, R. A., & Hallett, J. (1986). Observations of the distribution of ice in hurricanes. *Journal of the Atmospheric Sciences*, 43(8), 802-822. https://doi.org/10.1175/1520-0469(1986)043<0802:OOTDOI>2.0.CO;2

Blumberg, W. G., Halbert, K. T., Supinie, T. A., Marsh, P. T., Thompson, R. L. & Hart, J. A. (2017). SHARPpy: An open source sounding analysis toolkit for the atmospheric sciences. *Bulletin of the American Meteorological Society*. https://doi.org/10.1175/BAMS-D-15-00309.1

Boggs, L. D., Liu, N., Splitt, M., Lazarus, S., Glenn, C., Rassoul, H., & Cummer, S. A. (2016). An analysis of five negative sprite-parent discharges and their associated thunderstorm charge structures. *Journal of Geophysical Research: Atmospheres*, 121, 759–784, https://doi.org/10.1002/2015JD024188

Boggs, L. D., Liu, N., Riousset, J. A., Shi, F., Lazarus, S., Splitt, M., & Rassoul, H. K. (2018). Thunderstorm charge structures producing gigantic jets. *Scientific Reports*, 8(18085). https://doi.org/10.1038/s41598-018-36309-z

Boggs, L. D., Mach, D., Bruning, E., Liu, N., Van Der Velde, O., Montanyá, J. et al. (2022). Upward propagation of gigantic jets revealed by 3D radio and optical mapping. *Science Advances*, 8(31). https://doi.org/10.1126/sciadv.abl8731

Bruning, E. C., & MacGorman, D. R. (2013). Theory and observations of controls on lightning flash size spectra. *Journal of the Atmospheric Sciences*, 70, 4012-4029. https://doi.org/10.1175/JAS-D-12-0289.1

Carey, L. D., & Rutledge, S. A. (2000). The relationship between precipitation and lightning in tropical island convection: A C-Band Polarimetric Radar Study. *Monthly Weather Review*, 128(8), 2687-2710. https://doi.org/10.1175/1520-0493(2000)128<2687:TRBPAL>2.0.CO;2

Cecil, D. J., & Zipser, E. J. (1999). Relationships between tropical cyclone intensity and satellite-based indicators of inner core convection: 85-GHz ice-scattering signature and lightning. *Monthly Weather Review*, 127, 103–123. https://doi.org/10.1175/1520-0493(1999)127<0103:RBTCIA>2.0.CO;2

Cecil, D. J., Zipser, E. J., & Nesbitt, S. W. (2002). Reflectivity, ice scattering, and lightning characteristics of hurricane eyewalls and rainbands. Part I: Quantitative description. *Monthly Weather Review*, 130, 769–784. https://doi.org/10.1175/1520-0493(2002)130<0769:risalc>2.0.co;2

Chen, S. S., Knaff, J. A., & Marks, F. D., Jr. (2006). Effects of vertical wind shear and storm motion on tropical cyclone rainfall asymmetries deduced from TRMM. *Monthly Weather Review*, 134(11), 3190-3208. https://doi.org/10.1175/MWR3245.1

Chmielewski, V. C., Bruning, E. C., and Ancell, B. C. (2018). Variations of thunderstorm charge structures in West Texas on 4 June 2012. *Journal of Geophysical Research: Atmospheres, 123*, 9502–9523. https://doi.org/10.1029/2018jd029006

Corbosiero, K. L., & Molinari, J. (2002). The effects of vertical wind shear on the distribution of convection in tropical cyclones. *Monthly Weather Review*, 130(8), 2110–2123. https://doi.org/10.1175/1520-0493(2002)130⟨2110:TEOVWS⟩2.0.CO

Corbosiero, K. L., & Molinari, J. (2003). The relationship between storm motion, vertical wind shear, and convective asymmetries in tropical cyclones. *Journal of the Atmospheric Sciences*, 60(2), 366–376. https://doi.org/10.1175/1520-0469(2003)060⟨0366:TRBSMV⟩2.0.CO

Crum, T. D., & Alberty, R. L. (1993). The WSR-88D and the WSR-88D operational support facility. *Bulletin of the American Meteorological Society*, 74(9), 1669–1687. https://doi.org/10.1175/1520-0477(1993)074%3C1669:TWATWO%3E2.0.CO;2

Cullen, M. R. (2013). The Houston Lightning Mapping Array: Network installation and preliminary analysis. Master's thesis, Texas A & M University. Available electronically from https://hdl.handle.net/969.1/151109

Cummins, K. L., Krider, E. P., & Malone, M. D. (1998). The U.S. National Lightning Detection Network™ and applications of cloud-to-ground lightning data by electric power utilities. *IEEE Transactions on Electromagnetic Compatibility*, 40(4), 465–480. https://doi.org/10.1109/15.736207

DeHart, J. C., & Bell, M. M. (2020). A comparison of the polarimetric radar characteristics of heavy rainfall from Hurricanes Harvey (2017) and Florence (2018). *Journal of Geophysical Research: Atmospheres*, 125. https://doi.org/10.1029/2019jd032212

DeMaria, M., DeMaria, R. T., Knaff, J. A., & Molenar, D. (2012). Tropical cyclone lightning and rapid intensity change. *Monthly Weather Review*, 140, 1828–1842.

Didlake, A. C., & Kumjian, M. R. (2017). Examining polarimetric radar observations of bulk microphysical structures and their relation to vortex kinematics in Hurricane Arthur (2014). *Monthly Weather Review*, 145(11), 4521–4541. https://doi.org/10.1175/MWR-D-17-0035.1

Fierro, A. O., Mansell, E. R., Ziegler, C. L., & MacGorman, D. R. (2015). Explicitly simulated electrification and lightning within a tropical cyclone based on the environment of Hurricane Isaac (2012). *Journal of the Atmospheric Sciences*, 72, 4167–4193. https://doi.org/10.1175/jas-d-14-0374.1

Fierro, A. O., & Mansell, E. R. (2017). Electrification and lightning in idealized simulations of a hurricane-like vortex subject to wind shear and sea surface temperature cooling. *Journal of the Atmospheric Sciences*, 74, 2023–2041, https://doi.org/10.1175/JAS-D-16-0270.1

Frank, W. M., & Ritchie E. A. (2001). Effects of vertical wind shear on the intensity and structure of numerically simulated hurricanes. *Monthly Weather Review*, 129, 2249–2269. https://doi.org/10.1175/1520-0493(2001)129<2249:EOVWSO>2.0.CO;2

Fridlind, A. M., van Lier-Walqui, M., Collis, S., Giangrande, S. E., Jackson, R. C., Li, X., et al. (2019). Use of polarimetric radar measurements to constrain simulated convective cell evolution: A pilot study with Lagrangian tracking. *Atmospheric Measurement Techniques*, 12, 2979–3000. https://doi.org/10.5194/amt-12-2979-2019

Fuchs, B. R., Rutledge, S. A., Bruning, E. C., Pierce, J. R., Kodros, J. K., Lang, T. J., et al. (2015). Environmental controls on storm intensity and charge structure in multiple regions of the continental United States. *Journal of Geophysical Research: Atmospheres*, 120, 6575–6596. https://doi.org/10.1002/2015JD023271

Lu, G., Cummer, S. A., Lyons, W. A., Krehbiel, P. R., Li, J., Rison, W., et al. (2011). Lightning development associated with two negative gigantic jets, *Geophysical Research Letters*, 38, L12801, https://doi.org/10.1029/2011GL047662

Hallett, J., & Mossop, S. C. (1974). Production of secondary ice particles during the riming process. *Nature*, 249(5452), 26-28.

Han, Y., Luo, H., Wu, Y., Zhang, Y., & Dong, W. (2021). Cloud ice fraction governs lightning rate at a global scale. *Communications Earth and Environment*, 157 (2021). https://doi.org/10.1038/s43247-021-00233-4

Homeyer, C. R., & Bowman, K. P. (2017). Algorithm description document for version 3.1 of the three-dimensional Gridded NEXRAD WSR-88D Radar (GridRad) dataset. Technical Report.

Homeyer, C. R., Fierro, A. O., Schenkel, B. A., Didlake, A. C., Jr., McFarquhar, G. M., Hu, J. et al. (2021). Polarimetric Signatures in Landfalling Tropical Cyclones. *Monthly Weather Review*, 149(1), 131-154. https://doi.org/10.1175/MWR-D-20-0111.1

Hu, J., Rosenfeld, D., Ryzhkov, A., & Zhang, P. (2020). Synergetic use of the WSR-88D radars, GOES-R satellites, and lightning networks to study microphysical characteristics of hurricanes. *Journal of Applied Meteorology and Climatology*, 59, 1051–1068, https://doi.org/10.1175/jamc-d-19-0122.1

Kalnay, E., Kanamitsu, M., Kistler, R., Collins, W., Deaven, D., Gandin, L. et al. (1996). The NCEP/NCAR 40-Year reanalysis project. *Bulletin of the American Meteorological Society*, 77(3), 437-472. https://doi.org/10.1175/1520-0477(1996)077<0437:TNYRP>2.0.CO;2

Kaplan, J., & DeMaria, M. (2003). Large-scale characteristics of rapidly intensifying tropical cyclones in the North Atlantic basin. *Weather and Forecasting*, 18(6), 1093-1108. https://doi.org/10.1175/1520-0434(2003)018<1093:LCORIT>2.0.CO;2

Krehbiel, P. R., Thomas, R. J., Rison, W., Hamlin, T., Harlin, J., & Davis, M. (1999). Lightning mapping observations in central Oklahoma. *EOS*, 21-25.

Latto, A. S., & Berg, R. (2022). National Hurricane Center Tropical Cyclone Report: Hurricane Nicholas. https://www.nhc.noaa.gov/data/tcr/AL142021_Nicholas.pdf

Leighton, H., Black, R., Zhang, X., Marks, F. D., & Gopalakrishnan, S. G. (2020). Ice particle size distributions from composites of microphysics observations collected in tropical cyclones. *Geophysical Research Letters*, 47. https://doi.org/10.1029/2020GL088762

Liu, N., Spiva, N., Dwyer, J. R., Rassoul, H. K., Free, D., & Cummer, S. (2015). Upward electrical discharges observed above Tropical Depression Dorian. *Nature Communications*, 6 (5995). https://doi.org/10.1038/ncomms6995

Logan, T. (2021). An analysis of the performance of the Houston Lightning Mapping Array during an intense period of convection during Tropical Storm Harvey. *Journal of Geophysical Research: Atmospheres*, 126, e2020JD033270. https://doi.org/10.1029/2020JD033270

Lyons, W. A., Bruning, E. C., Warner, T. A., MacGorman, D. R., Edgington, S., Tillier, C., & Mlynarczyk, J. (2020). Megaflashes: Just how long can a lightning discharge get? *Bulletin of the American Meteorological Society*, 101(1), E73–E86. https://doi.org/10.1175/bams-d-19-0033.a

McCaul, E.W., Goodman, S. J., LaCasse, K.M., & Cecil, D. J. (2009). Forecasting lightning threat using cloud-resolving model simulations. *Weather and Forecasting*, 24(3), 709–729. https://doi.org/10.1175/2008WAF2222152.1

Mecikalski, R. M., Bain, A. L., & Carey, L. D. (2015). Radar and lightning observations of deep moist convection across Northern Alabama during DC3: 21 May 2012. *Monthly Weather Review*, 143(7), 2774-2794. https://doi.org/10.1175/MWR-D-14-00250.1

Medina, B. L., Carey, L. D., Lang, T. J., Bitzer, P. M., Deierling, W., & Zhu, Y. (2021). Characterizing charge structure in Central Argentina thunderstorms during RELAMPAGO utilizing a new charge layer polarity identification method. *Earth and Space Sciences*, 8, e2021EA001803.

Pan, B., Wang, Y., Logan, T., Hsieh, J.-S., Jiang, J. H., Li, Y., & Zhang, R. (2020). Determinant role of aerosols from industrial sources in Hurricane Harvey's catastrophe. *Geophysical Research Letters*, 47, e2020GL090014. https://doi.org/10.1029/2020GL090014

Petersen, W. A., & Rutledge, S. A. (2001). Regional variability in tropical convection: Observations from TRMM. *Journal of Climate*, 14, 3566–3586.

Peterson, M., Light, T. E. L., & Shao, X.-M. (2021). Combined optical and radio-frequency measurements of a lightning megaflash by the FORTE satellite. *Journal of Geophysical Research: Atmospheres*, 126(15), e2020JD034411. https://doi.org/10.1029/2020JD034411

Peterson, M. J., Lang, T. J., Logan, T., Wee Kiong, C., Gijben, M., Holle, R., et al. (2022). New WMO certified megaflash lightning extremes for flash distance and duration recorded from space. *Bulletin of the American Meteorological Society*, 103(4), 257–261. https://doi.org/10.1175/bams-d-21-0254.1

Peterson, M. (2023). A survey of thunderstorms that produce megaflashes across the Americas. *Earth and Space Science*, 10, e2023EA002920. https://doi.org/10.1029/2023EA002920

Qu, Z., Korolev, A., Milbrandt, J. A., Heckman, I., Huang, Y., McFarquhar, G. M., Morrison, H., Wolde, M., & Nguyen, C. (2022). The impacts of secondary ice production on microphysics and dynamics in tropical convection. *Atmospheric Chemistry and Physics*, 22, 12287–12310. https://doi.org/10.5194/acp-22-12287-2022

Rison, W., Thomas, R. J., Krehbiel, P. R., Hamlin, T., & Harlin, J. (1999). A GPS-based three-dimensional lightning mapping system: Initial observations in central New Mexico. *Geophysical Research Letters*, 26, 3573–3576.

Schultz, C. J., Carey, L. D., Schultz, E. V., & Blakeslee, R. J. (2015). Insight into the kinematic and microphysical processes that control lightning jumps. *Weather and Forecasting*, 30(6), 1591–1621. https://doi.org/10.1175/waf-d-14-00147.1

Shu, S., Feng, X., & Teng, D. (2021). Observed vertical structure of precipitation influenced by dry air for landfalling tropical cyclones over China. *Journal of Geophysical Research: Atmospheres*, 126, e2020JD034204. https://doi.org/10.1029/2020JD034204

Solorzano, N. N., Thomas, J. N., & Bracy, C. (2018). Monitoring tropical cyclones with lightning and satellite data. *EOS*, 99. https://doi.org/10.1029/2018EO092439

Steiger, S. M., Orville, R. E., & Carey, L. D. (2007). Total lightning signatures of thunderstorm intensity over North Texas. *Monthly Weather Review*, 135, 3281-3302.

Stevenson, S. N., Corbosiero, K. L., & Molinari, J. (2014). The convective evolution and rapid intensification of hurricane Earl (2010). *Monthly Weather Review*, 142(11), 4364–4380. https://doi.org/10.1175/MWR-D-14-00078.1

Stevenson, S. N., Corbosiero, K. L., & Abarca, S. F. (2016). Lightning in eastern North Pacific tropical cyclones: A Comparison to the North Atlantic. *Monthly Weather Review*, 144(1), 225-239. https://doi.org/10.1175/MWR-D-15-0276.1

Stolz, D. C., Businger, S., & Terpstra, A. (2014). Refining the relationship between lightning and convective rainfall over the ocean. *Journal of Geophysical Research: Atmospheres*, 119, 964-981. https://doi.org/10.1002/2012JD018819

Stolzenburg, M., & Marshall, T. C. (2009). Electric field and charge structure in lightning-producing clouds. *Lightning: Principles, Instruments and Applications*, H.-D. Betz, U. Schumann, P. Laroche (Eds.), Springer, Dordrecht. https://doi.org/10.1007/978-1-4020-9079-0_3

Takahashi, T. (1978). Riming electrification as a charge generation mechanism in thunderstorms. *Journal of the Atmospheric Sciences*, 35, 1536-1548.

Tessendorf, S. A., Rutledge, S. A., & Wiens, K. C. (2007). Radar and lightning observations of normal and inverted polarity multicellular storms from STEPS. *Monthly Weather Review*, 135, 3682-3706.

Thomas, R. J., Krehbiel, P. R., Rison, W., Hunyady, S. J., Winn, W. P., Hamlin, T., & Harlin, J. (2004). Accuracy of the lightning mapping array. *Journal of Geophysical Research*, 109, D14207. https://doi.org/10.1029/2004JD004549

Wadler, J. B., Cione, J. J., Zhang, J. A., Kalina, E. A., & Kaplan, J. (2022). The Effects of Environmental Wind Shear Direction on Tropical Cyclone Boundary Layer Thermodynamics and Intensity Change from Multiple Observational Datasets. Monthly Weather Review, 150(1), 115-134. https://doi.org/10.1175/MWR-D-21-0022.1

Wang, F., Liu, H., Dong, W., Zhang, Y., & Meng, Q. (2018). Characteristics of lightning flashes associated with the charge layer near the 0 °C isotherm in the stratiform region of mesoscale convective systems. *Journal of Geophysical Research: Atmospheres*, 123, 9524–9541. https://doi.org/10.1029/2018JD028569

Wang, Y., Lu, G., Peng, K.-M., Ma, M., Cummer, S. A., Chen, A. B., & Zhu, B. (2021). Space-based observation of a negative sprite with an unusual signature of associated sprite current. *Journal of Geophysical Research: Atmospheres*, 126, e2020JD033686. https://doi.org/10.1029/2020JD033686

Weiss, S. A., MacGorman, D. R., Bruning, E. C., & Chmielewski, V. C. (2018). Two Methods for Correcting Range-Dependent Limitations of Lightning Mapping Arrays. *Journal of Atmospheric and Oceanic Technology*, 35(6), 1273-1282. https://doi.org/10.1175/JTECH-D-17-0213.1

Wiens, K. C., Rutledge, S. A., & Tessendorf, S. A. (2005). The 29 June 2000 supercell observed during STEPS. Part II: Lightning and charge Structure. *Journal of the Atmospheric Sciences*, 62, 4151-4177.

Williams, E. R. (1985). Large-scale charge separation in thunderclouds. *Journal of Geophysical Research*, 90(D4), 6013–6025. https://doi.org/10.1029/JD090iD04p06013

Wood, K. M., & Ritchie, E. A. (2015). A definition for rapid weakening of North Atlantic and eastern North Pacific tropical cyclones. *Geophysical Research Letters*, 42, 10,091–10,097. https://doi.org/10.1002/2015GL066697

Xu, W., Rutledge, S. A., & Zhang, W. (2017). Relationships between total lightning, deep convection, and tropical cyclone intensity change. *Journal of Geophysical Research: Atmospheres*, 122, 7047–7063. https://doi.org/10.1002/2017JD027072